PCCP

Accepted Manuscript

ROYAL SOCIETY OF CHEMISTRY

www.rsc.org/pccp

Intrinsic Half-Metallicity in Fractal Carbon Nitride Honeycomb Lattices

Aizhu Wang, Mingwen Zhao*

School of Physics and State Key Laboratory of Crystal Materials, Shandong University, Jinan 250100, Shandong, China

Abstract

Fractal is a natural phenomenon that exhibits a repeating pattern “exactly the same at every scale or nearly the same at different scales”. The defect-free molecular fractals were assembled successfully in a recent literature [Shang et al., *Nature Chem*. 2015, **7**, 389-393]. Here, we adopted the feature of repeating pattern in searching for two-dimensional (2D) materials with intrinsic half-metallicity and high stability desirable for spintronics applications. Using first-principles calculations, we demonstrate that the electronic properties of fractal frameworks of carbon nitrides have stable ferromagnetism accompanied by half-metallicity, which are highly dependent on fractal structure. The ferromagnetism increases gradually with the increase of fractal order. The Curie temperature of these metal-free systems estimated from Monte Carlo simulations is much higher than room temperature. The stable ferromagnetism, intrinsic half-metallicity, and fractal characteristics of spin distribution in the carbon nitride frameworks open an avenue for the design of metal-free magnetic materials with exotic properties.

*E-mail: zmw@sdu.edu.cn

†Electronic supplementary information (ESI) available: fractal-like honeycomb model; the electrical properties of restructured g-$C_{13}N_9H_3$ and g-$C_{13}N_9H_3$ bulk materials; the electrical properties of high order (3^{rd} and 4^{th}) honeycomb lattice based on C_4N_3-H and C_4N_3-2H.

Introduction

Fractal[1], a natural phenomenon or a mathematical set, exhibits a repeating pattern that displays exactly the same at every scale or nearly the same at different scales, which occurs ubiquitously in nature and appears in different ways; examples from the physical and biological sciences include colloidal flocculation[2], percolation phenomena[3], and the structure of transport networks in organisms[4]. In the area of structural mechanics, fractal morphology of trabecular bone is expected to be responsible in part for its mechanical efficiency[5]. The flying buttresses and remarkably thin vaulted roofs of medieval European cathedrals are the striking examples for implements or buildings[6]. Recent theoretical work indicated that the scaling of material required for stability against loading can be altered by changing the fractal hierarchy of the structures[6-10]. The low density materials considered in that works look, when appropriately magnified, like a network of more or less regular hexagons[11]. So recent work has sought to improve the properties of such structures by hollowing out the elements and replacing them with repeating units[10]. More generalized two-dimensional (2D) honeycomb frameworks are predicted to have relatively high stiffness for their low density[12]. Oftadeh *et al.* considered a new family of honeycomb structures with a hierarchical refinement scheme, in which the structural hexagonal lattice is replaced by smaller hexagons[13] resembling the mathematical fractal set called as Sierpinski triangle. This process can be repeated to create frameworks of higher fractal hierarchy (see Fig. 1 and Fig. S1). In-plane stiffness and strength can be greatly improved in these cellular solids compared to the corresponding regular honeycombs[13,14].

Apart from mechanical properties of hexagon-based fractal frameworks, their electron spin-polarization and ferromagnetism, for example in graphite, is a topic of increasing interest, due to promising applications in organic spintronics devices. Pioneering works in this field include the electron spin-polarization of graphite, which is closely related to structures of vacancy defects[15, 16]. However, the fabrication of graphene nanomeshs with well-defined vacancies remains a big challenge in experiments. Graphitic carbon nitrides with natural porous frameworks[17-21] offer ideal candidate materials for the 2D fractal models. For example, the already-synthesized graphitic carbon nitride (g-C_4N_3) can be regarded as a member of Sierpinski honeycomb lattices with the hierarchy (n) of n=1[18, 22]. It has been demonstrated theoretically that the 1st order fractal lattice possesses an intrinsic half-metallicity, which is desirable for spintronics applications[18]. However, the study of the electronic properties of 2D fractal materials, especially the hierarchy-dependent feature, was still lacking.

In this contribution, we propose that fractal hierarchy is an interesting degree of freedoms in tuning the electronic properties of 2D materials. From first-principles calculations, we demonstrate that stable ferromagnetism and half-metallicity are the intrinsic features of the 2D graphitic carbon nitride materials with fractal characteristics in the unit cells, which are understandable in terms of the Lieb's theorem. The ferromagnetism increases gradually with the increase of fractal hierarchy. For the half-metallicity, the band gap of the semiconducting spin channel can be as wide as 2.67 eV. The Curie temperature (T_C~1105K) estimated by Monte Carlo simulations based on the Ising model is much higher than room temperature. Such exotic properties will be quite promising for applying the principle of topological frustration, such as the design of 2D fractal-like hierarchical structures with large spins or the context of circuits for spintronics and mechanical property applications.

Method and Computational Details

Our first-principles calculations were performed within the framework of density-functional theory (DFT), which is implemented in the Vienna ab initio simulation package known as VASP[23]. The electron-electron interactions were treated within a generalized gradient approximation (GGA) in form of Perdew-Burke-Ernzerhof (PBE) for the exchange-correlation functional[24]. The energy cutoff employed for plane-wave expansion of electron wavefunctions was set to 520 eV. The electron-ion interaction was described by projector-augmented-wave (PAW) potentials[25], including four electrons for carbon ($2s^22p^2$), five electrons for nitrogen ($2s^22p^3$) and one electron for hydrogen. The supercells with fractal features are repeated periodically on the x-y plane while a vacuum region of about 15 Å was applied along the z-direction to avoid mirror interaction between neighboring images. The Brillouin zone (BZ) integration was sampled on a grid of 9×9×1 k-points. Structural optimizations were carried out using a conjugate gradient (CG) method until the remaining force on each atom is less than 0.05 eV/ Å. Spin polarization is included through all the calculations. Since the DFT calculations within PBE functional always underestimated the electronic band gaps and may fail to describe electron spin-polarization, state-of-the-art hybrid Heyd-Scuseria-Ernzerhof (HSE06) functional[26] was also carried out to examine the magnetism and half-metallicity in a primitive of 1st and 2nd Sierpinski honeycomb lattices.

Results and discussion

The optimized fractal-like hierarchical Sierpinski triangles, as shown in Fig. 1, represent the component units of the 1st (g-C_4N_3) and 2nd (g-$C_{13}N_9H_3$) Sierpinski triangle honeycomb lattice. In the following parts, we take the 2nd Sierpinski honeycomb lattice as an example to discuss the structural and electronic properties of the 2D fractal carbon nitride materials. The results of the configurations with high fractal orders are presented in the ESI†. Different from the 1st honeycomb lattice, the inner connection of the 2nd honeycomb lattice is joined together via two C-C bonds with the need of additional carbon atoms, leading to a chemical formula of $C_{24}N_{18}H_6$ in a primitive cell. The planar configuration was preserved in the 2nd honeycomb lattice. The lengths of the C-N bonds in the triazinic (C3N3) ring range from 1.346 Å to 1.366 Å, which differ slightly from those in g-C_4N_3 (1.349 Å) and g-C_6N_6 (1.340 Å)[17], while the C-N-C bond angles are in range from 118.7° to 122.7°. The C-C bond length between the adjacent triazinic rings within a supercell is 1.418 Å, almost the same as that in graphene (1.420 Å), while the C-C-C bond angle, 122.2°, deviates slightly from the bond angle in graphene, 120°. This may be related to the polarization of the dangling bond electrons by the local strain and quantum entrapment of the core and bonding electrons at the edges[27].

The electronic structures of the 2nd honeycomb lattice are then calculated based on the optimized configurations. It is found that this configuration has a spin-polarized ground state with a magnetic moment of $4\mu_B$ in one unit cell, which is more stable than the spin-unpolarized state by about 0.34 eV. Fig. 2a gives the spin-resolved band structure of ferromagnetic 2nd honeycomb lattice in the vicinity of the Fermi level. Clearly, the Fermi level crosses bands in one spin channel (metallic) but resides at the band gap of the other channel (semiconducting), displaying the characteristics of half-metals. There are abundant states of the metallic channel while the band gap of the semiconducting channel is as large as 2.67 eV, as revealed by the spin-resolved electron density of states (DOS) shown in Fig. 2b, which facilitates fully spin-polarized carrier transportation. Notably, such half-metallicity is obtained without transition metals and external stimuli. Therefore, the 2nd honeycomb lattice appears as a fractal-like, metal-free, and half-metallic 2D material.

To visualize the spatial distribution of spins in this lattice, we plotted the spin-polarized electron density $\Delta\rho$, which were calculated from the difference between the electron density of two spin channels, $\Delta\rho = \rho_{\uparrow}-\rho_{\downarrow}$, in Fig. 2c. It is noteworthy that the shapes of the $\Delta\rho$ isosurfaces display features of p atomic orbitals, suggesting that the local magnetic moments come from the p electrons of C and N atoms. This is further confirmed by the orbital-resolved electron density of states (PDOS) projected onto C and N atoms, as shown in Fig. 3a-d. The electronic states, which are spin-polarized, arise mainly from the p_z atomic orbitals of C and N atoms and p_{xy} orbitals of N atoms.

The electron spin-polarization of the 2D fractal carbon nitride materials reminds us the graphene nanomeshs, which have nonzero magnetic moment dependent on their topological properties. Considerable efforts have been devoted to the intrinsic magnetic properties of graphene-derived structures. The triangular graphene quantum dots (QDs) with zigzag edges, resembling an artificial ferromagnetic atom, generally possesses a nonzero net spin, the value of which can be estimated by using the so-called Lieb's theorem[28] combined with a tight-binding approximation (TBA). In TBA, the secular equation reads: $Dx=Ex$, with D being the hopping matrix, E the eigenvalues and x the eigenvectors. The dimension of D equals to the number of atomic orbitals. It has nonzero elements only for the coupling orbitals on adjacent atoms. In special cases, D becomes singular and zero eigenvalues arise, which is called nonbonding states (NBSs)[29] or zero-energy states (ZES)[30]. The electron spin polarization in graphene QDs is related to the unbalance between the atoms belonging to the two sublattices of graphene. From a graph theory (GT) point of view, the number of positive (θ), negative (ν), and zero (η) eigenvalues of hopping matrix D are related to the maximum number of pairwise nonadjacent vertices α and edges β of graph G: $\alpha\ (G) = \beta\ (G) + \eta\ (G)$ and $\beta\ (G) = \theta\ (G) = \nu\ (G)$. η equals to the number of NBSs[29] or ZES[30]. The net spin (S) of a graphene QDs can be determined as $S = \eta/2 = (\alpha\text{-}\beta)/2 = \alpha\text{-}N/2$, where N is the total vertices that equals to the sum of θ, ν and η. The electron spin-polarization of graphene QDs with the so-called "Star of David" shape generated by repeatedly overlapping two triangles in opposite direction and removing the overlapped portions is a good example for this theorem[29].

The stable ferromagnetism in the 2D fractal carbon nitride materials is also understandable in terms of the above-mentioned theorem. It is found that the carbon atom in the nonadjacent vertices connecting two triazinic rings induces spin-polarized ground states with a local magnetic moment of 1.0 μ_B per unit, irrespective of the site. The corresponding magnetic moments increase gradually with the increased order of fractal as shown in Fig. 4a and Table 1. The electronic properties of high order (n=3 and 4) of C_4N_3-based fractals are presented in the ESI†. Interestingly, we also found that the total spin increases linearly with the fractal level n as $S_n = 3S_{n-1} + 0.5$ (n=2, 3, 4…). There are also two different strategies to describe the increased magnetic along the lines of the different units, more detail can be found in the ESI†. Obviously, the increased total spins, due to the increase of boundary length, is a hallmark of fractal structures. In our C_4N_3-based fractals, α is greater than the half population of the total atoms, resulting in a nullity and spin proportional to the total number of atoms due to the special configuration as in those graphene nanoflakes. To our surprise, the total spin also obeys the so-called Lieb's theorem[28,29], i.e., Sn = (N_A-N_B)/2, N_A and N_B are the number of A and B sublattices in one primitive cell. This is reasonable because the spin distribution in the fractal carbon nitrides resembles that of the fractal graphene nanoflakes, except the minor contribution of the p_{xy} orbitals of N atoms. Such features are more obvious in high order (n=4) due to the strengthening of p_z contribution. More information can be found in the ESI†.

The above calculations were performed using the primitive cells. In order to study the possible reconstruction and magnetic coupling between local magnetic moments; we adopted large-size supercells containing four primitive cells (denoted as (2×2)). Starting from different initial spin arrangements, self-consistent calculations lead to two types of magnetic orderings. One has the local magnetic moments aligned in a ferromagnetic way (FM), while, the other one has the local magnetic moments aligned in an "antiferromagnetic" way (AFM). Our calculations showed that the FM state of the 2nd honeycomb lattice is energetically more stable than the AFM state by about 287.17 meV per supercell. This implies that the local magnetic moments favor FM ordering at zero temperature with a total magnetic moment of 16.0 μ_B in the (2×2) supercell. Additionally, severe off-plane structural distortion took place in the (2×2) supercell, and the planar configuration became buckled as the 1st honeycomb lattices[18]. More information can be found in the ESI†. It is important to compare the relative stability between the (1×1) and (2×2) reconstructed structure. We found that the (2×2) reconstruction is energetically more stable by 0.21 eV per cell, indicating that the magnetism is robust against geometry relaxation in the supercell.

Finally, we evaluate the thermal stability of the ferromagnetism of the systems. The nearest-neighbor exchange parameter J_0 of the local magnetic moments can be evaluated using an Ising model. Without external filed, the Hamiltonian of the Ising model is written as

$$\hat{H} = -J_0 \sum_{i,j} \hat{m}_i \times \hat{m}_j \ ,$$

where $\hat{m}_i$ and $\hat{m}_j$ are the local magnetic moments at sites i and j. For the 2nd honeycomb lattice, J_0 can be evaluated from the energy difference between ferromagnetic configuration (FM) and antiferromagnetic configuration (AFM) states, $\Delta E = E_{FM} - E_{AFM}$ in a primitive cell, using the following formula: $J_0 = |\Delta E|/16m^2$. For each primitive cell, m =±4, J_0 was calculated to be about 1.12 meV. We also implement Monte Carlo (MC) simulations within the Ising Hamiltonian to study the tendency of magnetic moment as a function of temperature. We employ a 50×50 supercell containing 7500 local magnetic moments. The temperature-dependent magnetic moment per unit cell obtained from MC simulations is shown in Fig. 4b. Apparently the magnetic moment per unit cell becomes $0\mu_B$ when temperature is higher than 1105 K, indicating that the system undergoes a transition from FM to paramagnetic configuration (PM) with the temperature increasing. It is noteworthy that the structural distortion at high temperature which may reduce the magnetic moments of the systems and decrease the critical temperature was not taken into account. Therefore, the high Curie temperature predicted from the MC simulations may be overestimated. Anyway, such a high Curie temperature ensures a high stability of FM states at room temperature.

Apart from above C_4N_3-H-based fractals, we also consider other model fractal-like honeycomb lattices (C_4N_3-2H-based fractals) by using two hydrogen atoms to replace a hydrogen atom shown in Fig. 5. The stoichiometry of the 2nd honeycomb lattice is $C_{13}N_9H_6$, and the optimized lattice constant is 9.808 Å. Similar to the case of the $C_{13}N_9H_3$ lattice, the $C_{13}N_9H_6$ honeycomb lattice also has a perfect planner configuration. Stable ferromagnetism can be achieved with 1 μ_B magnetic moment in one primitive cell. Ferromagnetic $C_{13}N_9H_6$ honeycomb is also half-metal with a Curie temperature of 370 K. Different from the model of C_4N_3-H-based fractals, the total magnetic moments is $1\mu_B$, independent of the order of fractal. The half-metal state confirms that it is the intrinsic property of the metal-free fractal-like honeycomb lattices, which would bring about interesting mechanical properties of those structures. More details of electronic properties of high order (n=3 and 4) of C_4N_3-2H-based fractals can be can be found in the ESI†.

It is well known that the general gradient approximation (Perdew-Burke-Ernzerhof exchange correlation functional) always significantly underestimate the band gap semiconductors and overestimate the ferromagnetic coupling strength[31]. More accurate functional, such as HSE06 hybrid functional[26] is expected to give reasonable prediction. To confirm the robustness of the half-metallicity, we also performed HSE hybrid functional calculations. Because of computational limitations for the large systems, we calculated only parts of the band structure of the g-C_4N_3 and g-$C_{13}N_9H_3$ honeycomb lattices shown in Fig. 6a and 6b. Clearly, both functional give similar dispersion curves for valence and conduction bands, respectively, but the position of conduction bands is significantly up-shifted. Remarkably, the ground state still remains ferromagnetic with the same magnetic moment as that obtained by the Perdew-Burke-Ernzerhof (PBE) exchange correlation functional. So the predicted intrinsic half-metallicity and ferromagnetism survive to the choice of functional.

Here, we also comment on possibility for synthesizing fractal carbon nitride honeycomb structures. On the one hand, we test the stability of fractal carbon nitride honeycomb framework by calculating the formation energy with respect to the denser (and existing) g-C_4N_3 structure. Because they have different stoichiometries, the energetic stability is dependent on the chemical potentials of carbon (μ_C), hydrogen (μ_H) atoms and the total energies of g-C_4N_3. Here, we defined the formation energy (ΔE) as:

$$\Delta E=\frac{[E_{total}[C_aN_bH_c]-(a-4x)*\mu_C-c*\mu_H-x*E_{total}[C_4N_3]]}{(a+b+c)}$$

where E_{total} represent the total energies of the carbon nitride materials with different order, μ_C and μ_H are the chemical potentials of carbon and hydrogen atoms. a, b, c and x are the number of carbon atoms, nitrogen atoms, hydrogen atoms and C_4N_3 units. Under carbon-rich conditions, μ_C was calculated from graphene. Under hydrogen-rich condition, μ_H was calculated from a H_2 molecule in gas phase. In both cases, μ_C and μ_H are linked by the thermodynamic constraint, $\mu_C+4\mu_H=E_{CH_4}$, where E_{CH_4} is the total energy of a CH_4 molecule which is a stable form of hydrocarbon. The formation energies of C_4N_3-H-based and C_4N_3-2H-based fractals are listed in Table 1. Although the value of formation energy depends on the definition itself, the negative formation energies of the C_4N_3-2H-based fractals framework suggest its high plausibility.

Finally, we focus on the possible routes for synthesizing fractal carbon nitride honeycomb structures. With the increase of fractal order, the size of the voids involved becomes larger, which is disadvantageous for the stability of the lattice. However, this can be solved by growing the fractal carbon nitrides on substrates. As far as our knowledge, numerous fractal objects created by atoms and molecules at interfaces, such as diffusion limited aggregation clusters or atomic islands from molecular beam epitaxy, which are repeating in a statistical sense, have been observed to date[32,33]. The creation of repeating 2D fractal aggregates based on Sierpinski triangle has been systematically designed and realized in experiments including DNA tiles on mica[34], while bis-terpyridine building blocks co-adsorbed with Ru and Fe on the Au (111) surface[35], which show the possibility of hierarchical fractal structures, have been assembled the Sierpinski triangle in experimental systems. Interestingly, a previous study showed that the linear counterpart, 4,4''-dibromop-terphenyl, can be self-assembled into a planar porous network with triangular voids via cyclic halogen-bonding nodes[36, 37]. A following literature demonstrated that it is critical to achieve a subtle balance between the mobility of the assembling molecular and the stability of the assembled fractals to realize an unfauled chiral connection and defect-free fractals[38, 39]. The synthetized of planar and defect-free fractals stimulate us to get a smoothness of our fractal structures. To our exciting, though the reconstructed (2×2) 2nd honeycomb lattice is buckled, the planar configuration will be preserved when the unit cell becomes larger. More detail can be found in the ESI†. More importantly, carbon nitrides (CNs) have been synthesized by supramolecular aggregation followed by ionic melt polycondensation (IMP) using melamine and 2,4,6-triaminopyrimidine as dopants[40], paving a way for realizing real 2D fractal carbon nitride structures.

Conclusions

Using first-principles calculations, we demonstrate that the electronic properties of fractal frameworks of carbon nitrides are dependent on the fractal model. Half-metallicity and stable ferromagnetism can be achieved in C_4N_3-based fractals. The Curie temperature of these metal-free systems can be as large as 1105 K. More importantly, the magnetic moment increase gradually with the increased order of fractal. In general, the principle of fractal can be used to induce large spin and interesting spin distributions in the framework of carbon nitrides, which opens an avenue for the design of a family of metal-free half-metal fractal structures.

Acknowledgements

This work is supported by the National Basic Research Program of China (No.2012CB932302), the National Natural Science Foundation of China (Nos.91221101, 21433006), the 111 project (No.B13029), the Taishan Scholar Program of Shandong, and National Super Computing Centre in Jinan.

References

1 B. B. Mandelbrot, *The Fractal Geometry of Nature* (W. H. Freeman, New York, 1983).

2 Y. Kantor, I. Webman, *Phys. Rev. Lett.,* 1984, **52**, 1891-1894.

3 M. B. Isichenko, *Rev. Mod. Phys.,* 1992, **64**, 961-1043

4 G. B. West. J. H. Brown, B. J. Enquist, *Science,* 1997, **276**, 122-126.

5 R. Huiskes, R. Ruimerman, GH. Van Lenthe, JD. Janssen. *Nature* (London), 2000, **405**, 704.

6 R. Farr, *Phys. Rev. E,* 2007, **76**, 046601.

7 R. Farr, *Phys. Rev. E,* 2007, **76**, 056608.

8 R. Farr and Y. Mao, *EPL*, 2008, **84**, 14001.

9 D. Rayneau-Kirkhope, R. S. Farr and Y. Mao, *EPL,* 2011, **93**, 34002.

10 D. Rayneau-Kirkhope, Y. Mao and R. S. Farr, *Phys. Rev. Lett.,* 2012, **109**, 204301.

11 L. J. Gibson, M. F. Ashby, G. S. Schajer, C. I. Robertson, *Proc. R. Soc. London A,* 1982, **382**, 43-59.

12 L. J. Gibson and M. F. Ashby, *Cellular Solids: Structure and Properties* (Cambridge University Press, Cambridge, England, 1999).

13 R. Oftadeh, B. Haghpanah, D. Vella, A. Boudaoud and A. Vaziri, *Phys. Rev. Lett.,* 2014, **113**, 104301.

14 B. Haghpanah, R. Oftadeh, J. Papadopoulos and A. Vaziri, *Proc. R. Soc. A,* 2013, **469**, 0022.

15 H. H. Xia, W. F. Li, Y. Song, X. M. Yang, X. D. Liu, M. W. Zhao, Y. Y. Xia, C. Song, T. W. Wang, D. Z. Zhu, J. L. Gong and Z. Y. Zhu, *Adv. Mater.,* 2008, **20**, 4679-4683.

16 X. M. Yang, H. H. Xia, X. B. Qin, W. F. Li, Y. Y. Dai, X. D. Liu, M. W. Zhao, Y. Y. Xia, S. S. Yan and B. Y. Wang, *Carbon*, 2009, **47**, 1399-1406.

17 A. Z. Wang, X. M. Zhang M. W. Zhao, *Nanoscale*, 2014, **6**, 11157-11162.

18 A. J. Du, S. Sanvito and S. C. Smith, *Phys. Rev. Lett.,* 2012, **108**, 197207.

19 Y. Wang, X. Wang and M. Antonietti, *Angew. Chem. Int. Ed.,* 2012, **51**, 68-89.

20 X. Zhang, M, Zhao, A. Wang, X. Wang and A. Du, *J. Mater. Chem. C*, 2013,**1**, 6265-6270.

21 X. Zhang, A. Wang and M. Zhao, *Carbon,* 2015, **84**, 1-8.

22 J. S. Lee, X. Wang, H. Luo and S. Dai, *Adv. Mater.*, 2010, **22**, 1004-1007.

23 G. Kresse, and J. Furthmuller, *Phys. Rev. B: Condens. Matter Mater. Phys,* 1996, **54**, 11169-11186.

24 J. P. Perdew, K. Burke and M. Ernzerhof, *Phys. Rev. Lett.,* 1996, **77**, 3865-

3868.

25 G. Kresse and D. Joubert, *Phys. Rev. B: Condens. Matter Mater. Phys.,* 1999, **59**, 1758.

26 J. Heyd, G. E. Scuseria and M. Ernzerhof, *J. Chem. Phys.,* 2006, **124**, 219906.

27 C. Q. Sun, *Springer Series of Chem Phys, Relaxation of the Chemical Bond, part II*, 2014, vol. 108, pp. 239–249.

28 E. Lieb, *Phys. Rev. Lett.,* 1989, **62**, 1201-1204.

29 W. L. Wang, S. Meng and E. Kaxiras, *Nano letter*, 2008, **8**, 241-245.

30 A. Wang, M. Zhao, Y. Xi, X. Wang, and Z. Wang, *Phys. Lett. A*, 2013, **377**, 1102-1108.

31 X. Wang, M. Zhao, T. He, Z. Wang and X. Liu, *Appl. Phys. Lett.*, 2013, **102**, 062411.

32 D. Nieckarz and P. Szabelski, *Chem. Commun.,* 2014, **50**, 6843-6845.

33 A. -L. Barabasi and H. E. Stanley, *Fractal concepts in surface growth,* Cambridge University Press, Cambridge, 1995; *The fractal approach to heterogeneous chemistry*, D. Avnir, J. Wiley and S. Ltd, New York, 1989.

34 F. Kenichi, H. Rizal, H. Sung, W Erik and M. Satoshi, *Nano Lett.,* 2008, **8**, 1791.

35 G. R. Newkome, P. Wang, C. N. Moorefield, T. J. Cho, P. P. Mohapatra, S. Li, S.-H. Hwang, O. Lukoyanova, L. Echegoyen, J. A. Palagallo, V. Iancu and S-W. Hla, *Science*, 2006, **312**, 1782.

36 W. Wang, X. Shi, S. Wang, M. A. Van Hove & N. Lin, *J. Am. Chem. Soc.* 2011, **133**, 13264-13267.

37 J. Shang, et al. *Nature Chem*. 2015, **7**, 389-393.

38 H. Brune, C. Romainczyk, H. Röder & K. Kern, *Nature* 1994, **369**, 469–471.

39 R. Otero, et al. *Science* 2008, **319**, 312–315.

40 M. K. Bhunia, K.Yamauchi and K. Takanabe, *Angew. Chem. Int. Ed.* 2014, **53**, 11001-11005.

Abstract Figure

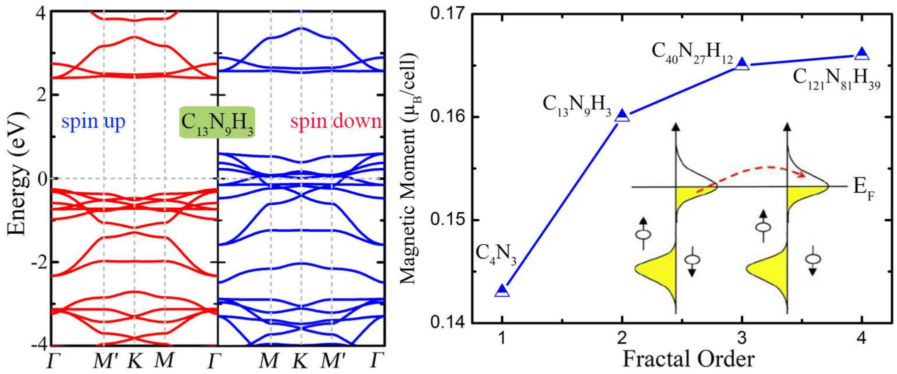

Table 1

The chemical formulas, lattice constants (Å), fractal dimensions, magnetic moments (μ_B), electronic properties with Half-metallicity (H-M) and the formation energies of different models based on C_4N_3-H and C_4N_3-2H.

Model	Fractal Hierarchy	Chemical Formula	Lattice Constant (Å)	Fractal Dimension	Magnetic Moments (μ_B)	Electronic Property	Formation Energy (eV/atom)	
							H-rich	C-rich
C_4N_3 (H)	1st	C_4N_3	4.838	ln(2)/ln(3) =1.58	1	H-M	0.000	0.000
	2nd	$C_{13}N_9H_3$	9.678		4	H-M	0.058	0.053
	3rd	$C_{40}N_{27}H_{12}$	19.142		13	H-M	0.063	0.057
	4th	$C_{121}N_{81}H_{39}$	41.880		40	H-M	0.587	0.580
C_4N_3 (2H)	1st	C_4N_3	4.838	ln(2)/ln(3) =1.58	1	H-M	0.000	0.000
	2nd	$C_{13}N_9H_6$	9.808		1	H-M	-0.081	-0.072
	3rd	$C_{40}N_{27}H_{24}$	19.212		1	H-M	-0.092	-0.081
	4th	$C_{121}N_{81}H_{78}$	39.902		1	H-M	-0.107	-0.095

Figure caption

Fig.1

(a) (Color online) Schematic representations of unit cell of the Sierpinski triangle with regular structure (left) and with first order hierarchy (right). (b) Schematic representation the real materials of the fractal-like hierarchical Sierpinski triangle lattice (1st) and its next order (2nd).

Fig. 2

(a) (Color online) Spin-resolved band structures of 2nd honeycomb lattice. Spin-up and spin-down channels are represented by red lines and blue lines, respectively. (b) Spin-resolved total electron density of states of the 2nd honeycomb lattice. The energy at the Fermi level was set to zero. (c) Spin-polarized electron density isosufaces of the 2nd honeycomb lattice. (d) Enlarged view to the electron density. (e) Schematic representation of the exchange mechanisms. Virtual hopping results in a ferromagnetic ground state.

Fig. 3

Orbital resolved electron density of states projected onto (a) C_1, (b) C_2, (c) N_1 and (d) N_2 atoms. Spin-up and spin-down channels are plotted in the top and bottom panels, respectively. The p_z orbitals contribute mostly to the electronic states in proximity of Fermi level are marked by green solid lines combined with solid area for the occupied states. The energy at the Fermi level was set to zero.

Fig. 4

(a) The magnetic moment increase gradually with the increased order of fractal. The 1st and 4th order Sierpinski triangles are shown in the inset of this figure. (b) Monte Carlo simulations of the average magnetic moment in primitive cell of 2nd honeycomb lattice as a function of temperature. The primitive cell of 2nd honeycomb lattice is shown in the inset of this figure.

Fig. 5

(a) Schematic representation the real materials of the fractal-like hierarchical Sierpinski triangle lattice (2nd) with the stoichiometry of $C_{13}N_9H_6$. (b) (Color online) Spin-resolved band structures of g-$C_{13}N_9H_6$ honeycomb lattice. Spin-up and spin-down channels are represented by red lines and blue lines, respectively. Spin-resolved total electron density of states was listed in the right column. The energy at the Fermi level was set to zero. (c) Spin-polarized electron density isosufaces of g-$C_{13}N_9H_6$ honeycomb lattice. (d) Monte Carlo simulations of the average magnetic moment in primitive cell of g-$C_{13}N_9H_6$ honeycomb lattice as a function of temperature.

Fig. 6

Spin-polarized band structures of the 1st (g-C_4N_3) and 2nd (g-$C_{13}N_9H_3$) honeycomb lattices obtained from PBE and HSE calculations. Red lines are spin-up channels, and blue ones are spin-down channels. The energy at the Fermi level was set to zero.

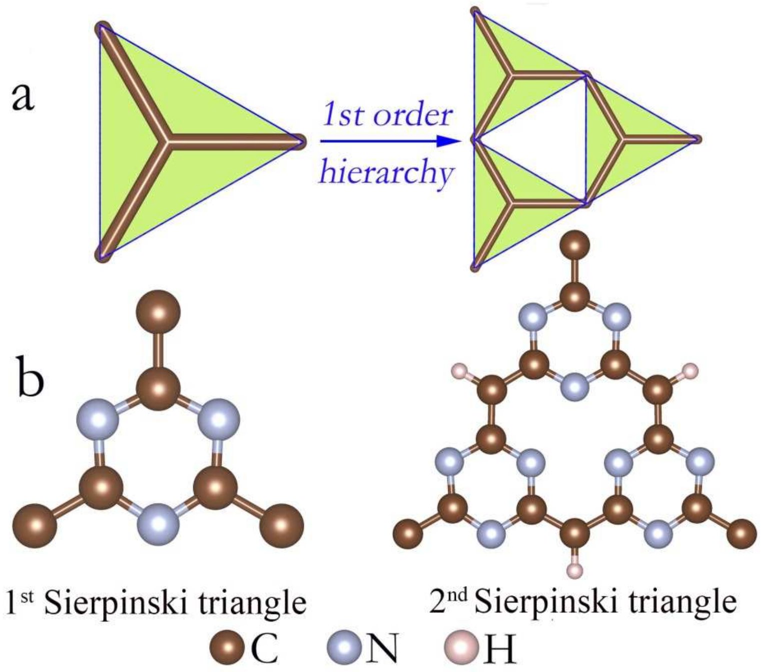

Fig.1

(a) (Color online) Schematic representations of unit cell of the Sierpinski triangle with regular structure (left) and with first order hierarchy (right). (b) Schematic representation the real materials of the fractal-like hierarchical Sierpinski triangle lattice (1^{st}) and its next order (2^{nd}).

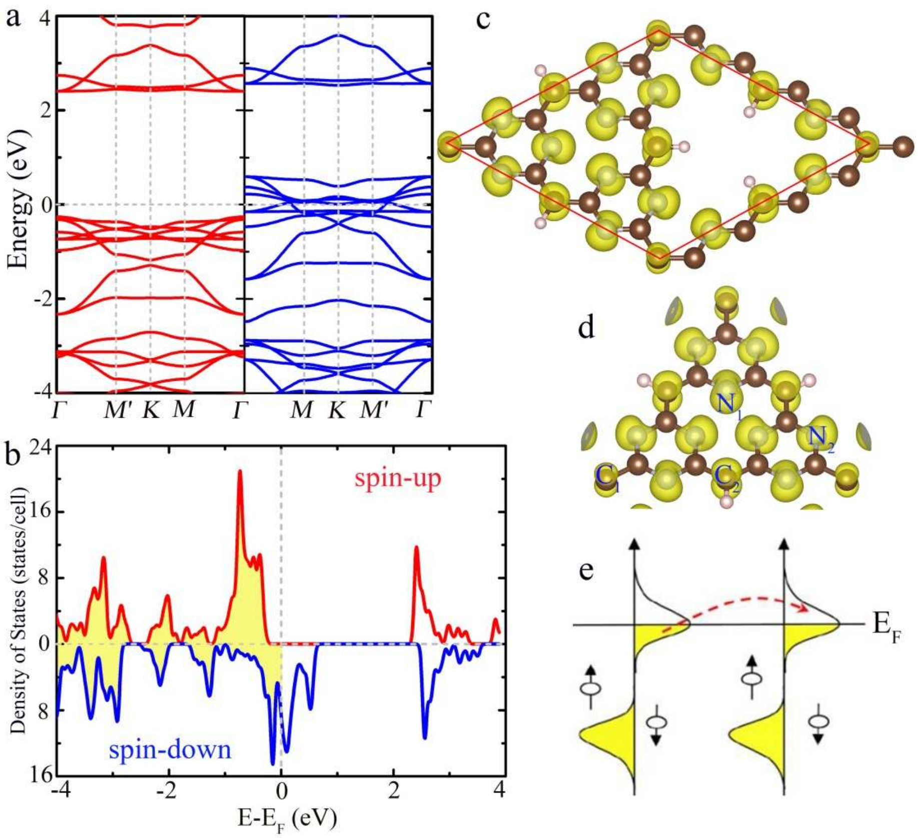

Fig. 2

(a) (Color online) Spin-resolved band structures of 2nd honeycomb lattice. Spin-up and spin-down channels are represented by red lines and blue lines, respectively. (b) Spin-resolved total electron density of states of the 2nd honeycomb lattice. The energy at the Fermi level was set to zero. (c) Spin-polarized electron density isosufaces of the 2nd honeycomb lattice. (d) Enlarged view to the electron density. (e) Schematic representation of the exchange mechanisms. Virtual hopping results in a ferromagnetic ground state.

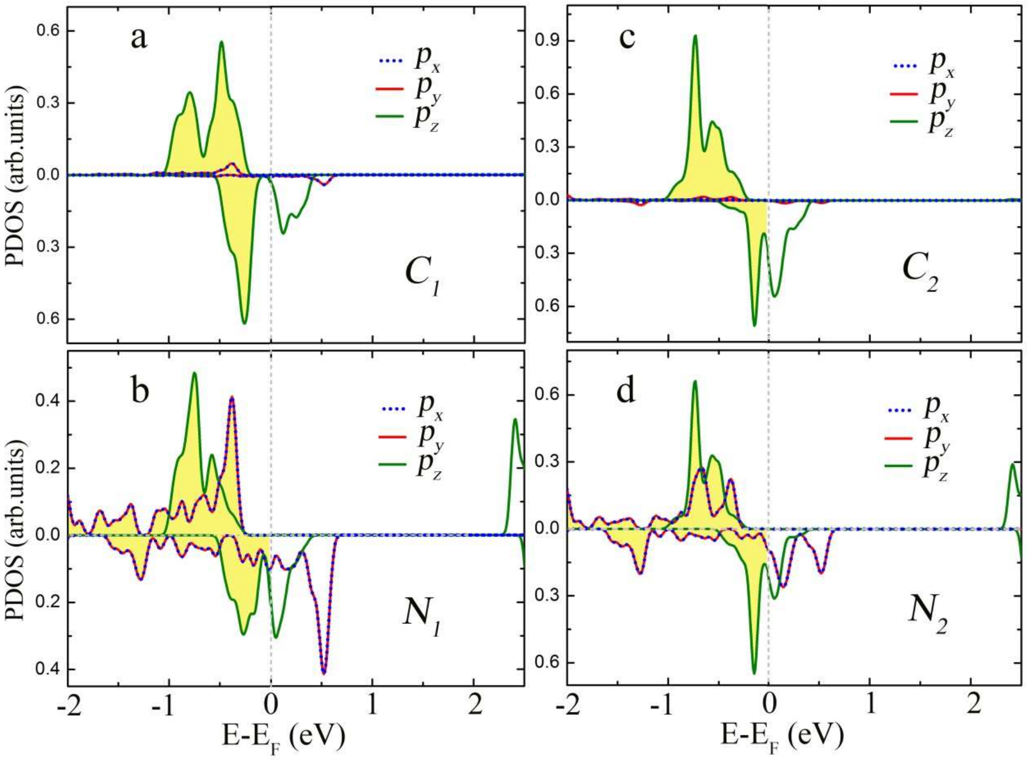

Fig. 3

Orbital resolved electron density of states projected onto (a) C_1, (b) C_2, (c) N_1 and (d) N_2 atoms. Spin-up and spin-down channels are plotted in the top and bottom panels, respectively. The p_z orbitals contribute mostly to the electronic states in proximity of Fermi level are marked by green solid lines combined with solid area for the occupied states. The energy at the Fermi level was set to zero.

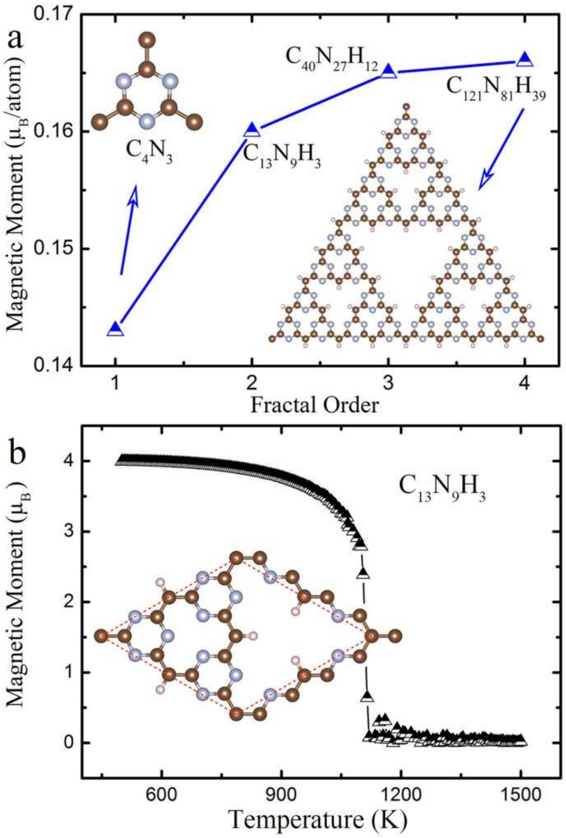

Fig. 4

(a) The magnetic moment increase gradually with the increased order of fractal. The 1st and 4th order Sierpinski triangles are shown in the inset of this figure. (b) Monte Carlo simulations of the average magnetic moment in primitive cell of 2nd honeycomb lattice as a function of temperature. The primitive cell of 2nd honeycomb lattice is shown in the inset of this figure.

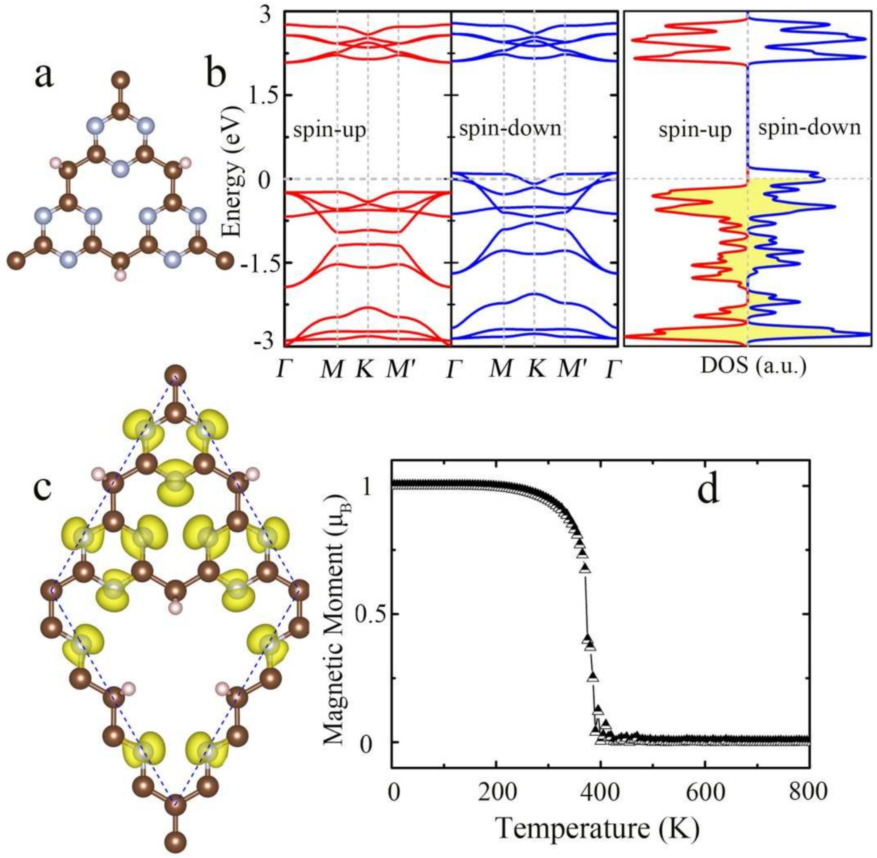

Fig. 5

(a) Schematic representation the real materials of the fractal-like hierarchical Sierpinski triangle lattice (2^{nd}) with the stoichiometry of $C_{13}N_9H_6$. (b) (Color online) Spin-resolved band structures of g-$C_{13}N_9H_6$ honeycomb lattice. Spin-up and spin-down channels are represented by red lines and blue lines, respectively. Spin-resolved total electron density of states was listed in the right column. The energy at the Fermi level was set to zero. (c) Spin-polarized electron density isosufaces of g-$C_{13}N_9H_6$ honeycomb lattice. (d) Monte Carlo simulations of the average magnetic moment in primitive cell of g-$C_{13}N_9H_6$ honeycomb lattice as a function of temperature.

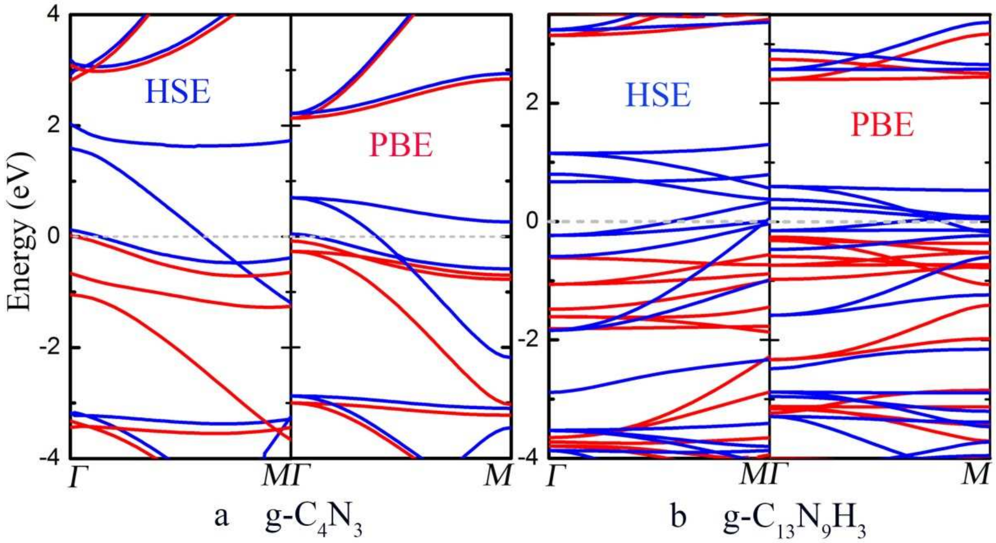

Fig. 6

Spin-polarized band structures of the 1st (g-C_4N_3) and 2nd (g-$C_{13}N_9H_3$) honeycomb lattices obtained from PBE and HSE calculations. Red lines are spin-up channels, and blue ones are spin-down channels. The energy at the Fermi level was set to zero.